Water in the atmosphere of HD 209458b from 3.6–8 μm IRAC photometric observations in primary transit

J. P. Beaulieu,[1,2]*† D. M. Kipping,[2]* V. Batista,[1]* G. Tinetti,[2]* I. Ribas,[3] S. Carey,[4]
J. A. Noriega-Crespo,[4] C. A. Griffith,[5] G. Campanella,[2,6] S. Dong,[7] J. Tennyson,[2]
R. J. Barber,[2] P. Deroo,[8] S. J. Fossey,[2] D. Liang,[9,10] M. R. Swain,[8] Y. Yung[10]
and N. Allard[1,11]

[1]*Institut d'Astrophysique de Paris, CNRS, UMR7095, Université Paris VI, 98bis Boulevard Arago, Paris, France*
[2]*Department of Physics and Astronomy, University College London, Gower Street, London WC1E 6BT*
[3]*Institut de Ciencies de l'Espai (CSIC-IEEC), Campus UAB, 08193 Bellaterra, Spain*
[4]*IPAC-Spitzer Science Center, California Institute of Technology, Pasadena, CA 91125, USA*
[5]*Department of Planetary Sciences, Lunar and Planetary Laboratory, The University of Arizona, Tucson, AZ 85721-0092, USA*
[6]*Dipartimento di Fisica, Università di Roma 'La Sapienza', Ple Aldo Moro 5, 00185 Rome, Italy*
[7]*Ohio State University, Colombus, OH 43210, USA*
[8]*Jet Propulsion Laboratory, California Institute of Technology, 4800 Oak Grove Drive, Pasadena, CA 91109-8099, USA*
[9]*Research Centre for Environmental Changes, Academia Sinica, Taipei, Taiwan*
[10]*Division of Geological and Planetary Sciences, California Institute of Technology, Pasadena, CA 91125, USA*
[11]*GEPI, Observatoire de Paris, 77 Avenue Denfert Rochereau, 75014 Paris, France*

ABSTRACT

The hot Jupiter HD 209458b was observed during primary transit at 3.6, 4.5, 5.8 and 8.0 μm using the Infrared Array Camera (IRAC) on the *Spitzer Space Telescope*. We describe the procedures we adopted to correct for the systematic effects present in the IRAC data and the subsequent analysis. The light curves were fitted including limb-darkening effects and fitted using Markov Chain Monte Carlo and prayer-bead Monte Carlo techniques, obtaining almost identical results. The final depth measurements obtained by a combined Markov Chain Monte Carlo fit are at 3.6 μm, 1.469 ± 0.013 and 1.448 ± 0.013 per cent; at 4.5 μm, 1.478 ± 0.017 per cent; at 5.8 μm, 1.549 ± 0.015 per cent; and at 8.0 μm, 1.535 ± 0.011 per cent. Our results clearly indicate the presence of water in the planetary atmosphere. Our broad-band photometric measurements with IRAC prevent us from determining the additional presence of other molecules such as CO, CO_2 and methane for which spectroscopy is needed. While water vapour with a mixing ratio of 10^{-4} to 10^{-3} combined with thermal profiles retrieved from the day side may provide a very good fit to our observations, this data set alone is unable to resolve completely the degeneracy between water abundance and atmospheric thermal profile.

Key words: techniques: photometric – occultations – planets and satellites: general – planetary systems.

1 INTRODUCTION

More than 420 exoplanets, i.e. planets orbiting a star other than our Sun, are now known thanks to indirect detection techniques (Schneider 2009). In the first decade after the initial discovery of a hot Jupiter orbiting a solar-like star in 1995 (Mayor & Queloz 1995), the task was to find more and more of these astronomical bodies. In recent years, attention has switched from finding planets to characterizing them. Among the variety of exoplanets discovered, particular attention is being devoted to those planets that transit their parent star, and whose presence can therefore be detected by a reduction in the brightness of the central star as the planet passes in front of it. 69 of the 420+ currently identified exoplanets are transiting planets, and for these objects planetary and orbital parameters such as radius, eccentricity, inclination, mass (given by radial velocity combined measurements) are known, allowing first-order characterization on the bulk composition and temperature. In particular, it is possible to exploit the wavelength dependence of

---

*HOLMES Collaboration.
†E-mail: beaulieu@iap.fr

this extinction to identify key chemical components in the planetary atmosphere (Seager & Sasselov 2000; Brown 2001), which permits enormous possibilities for exoplanet characterization.

The extrasolar planet HD 209458b orbits a main-sequence G star at 0.046 au (period 3.52 d). It was the first exoplanet for which repeated transits across the stellar disc were observed (~1.5 per cent absorption; Charbonneau et al. 2000). Using radial velocity measurements (Mazeh et al. 2000), the planet's mass and radius were able to be determined ($M_p \sim 0.69\, M_{Jup}$, $R_p \sim 1.4\, R_{Jup}$), confirming the planet is a gas giant with one of the lowest densities so far discovered. Consequently it must possess a highly extended atmosphere making it one of the optimum candidates for observation using primary transit techniques, and it was indeed the first exo-atmosphere probed successfully using this method in the visible (Charbonneau et al. 2002) and then in the infrared (IR) (Richardson et al. 2006).

Following the work on HD 189733b, where the first detections of water vapour (Tinetti et al. 2007b; Beaulieu et al. 2008) and methane (Swain, Vasisht & Tinetti 2008) have been achieved, we were awarded 20 h Director's Discretionary Time on *Spitzer* (PI Tinetti, WETWORLD, PID 461) to probe the atmosphere of HD 209458b in primary transit in the four Infrared Array Camera (IRAC) bands at 3.6, 4.5, 5.8 and 8 μm (channels 1 to 4, respectively). Water vapour was proposed to be present in the atmosphere of HD 209458b by Barman (2007), to fit the data recorded by *Hubble*-STIS in the visible (Knutson et al. 2007). Also, water vapour combined with a thermal profile increasing with altitude was a reasonable explanation to fit the secondary transit photometric data observed in the mid-IR (Deming et al. 2005; Burrows et al. 2007; Knutson et al. 2007). Our understanding of the thermal profile and composition has improved thanks to more recent secondary transit spectroscopic data in the near- and mid-IR, indicative of the additional presence of methane and carbon dioxide in the atmosphere of HD 209458b (Swain et al. 2009b), confirmed by Madhusudhan & Seager (2009).

Transmission and emission spectra probe different regions of a hot-Jupiter atmosphere, both longitudinally and vertically (Tinetti & Beaulieu 2008). In particular, the mid-IR primary transit observations described here allow us to probe the terminator region of HD 209458b between the bar and millibar level.

2 OBSERVATIONS AND DATA REDUCTION

2.1 Planning the observations

Three HD 209458 primary transits were observed with the IRAC camera on board the *Spitzer Space Telescope*. Channels 1 and 3 (3.6 and 5.8 μm) were observed at two epochs, on 2007 December 30 and 2008 July 18, and data were obtained using channels 2 and 4 (4.5 and 8 μm) on 2008 July 20. Since HD 209458 is a G0V star with a Two Micron All Sky Survey (2MASS) K_s magnitude of 6.3, the IRAC predicted fluxes are 878, 556, 351 and 189 mJy in channels 1–4, respectively. For our observations we required extremely high signal-to-noise ratio as the modelled contribution to the absorption due to H_2O was predicted to be a few $\times 10^{-4}$ of the stellar flux.

As with other *Spitzer* observations of transiting planets, it is necessary to observe the target continuously without dithering, in order to be able to quantify optimally the systematic effects detailed below.

(i) Flat-fielding errors are an important issue; observations at different positions on the array effectuate systematic scatter in the photometric data that can potentially swamp the signal that we are looking for.

(ii) The amount of light detected in channels 1 and 2 shows variability that depends on the relative position of the source with respect to the pixel centre (labelled the pixel phase effect). The time-scale of this variation is of the order of 50 min. These effects are well known and documented in the IRAC Data Handbook and also discussed by Morales-Calderón (2006), Beaulieu et al. (2008), Knutson et al. (2008) and Agol et al. (2008). To first order, these are able to be corrected for using the prescription of Morales-Calderón (2006). However, as the effects are variable across the array, ultimately they have to be estimated from the data themselves.

(iii) In channels 3 and 4 there are only minor pixel phase effects, but a variation of the response of the pixels to a long period of illumination and latent build-up effect impinge on the 5.8 and 8.0-μm observations, respectively.

(iv) We obtained a slightly longer 'pre-transit' data set, in order to allow the satellite settle in a 'repeatable' jitter pattern and a shorter post-transit data set. The time-scale of the pixel-phase effect being of the order of 50 min, we chose 120 min of pre-transit and 80 min of post-transit data baseline.

It is important to note that the ~184 min transit of HD 209458b means that our data contain three full cycles of the pixel phase variation in the transit itself, giving an excellent opportunity to have a full control on the behaviour of the systematic effects by evaluating them both in and outside the transit.

Our observations employed the IRAC 0.4/2 second stellar photometry mode. Using the regular Astronomical Observation Templates (AOTs), a total of two transits per field of view was required to achieve the desired sensitivity at 4.5 and 5.8 μm (the arrays with the limiting sensitivity). Unfortunately, the AOTs as designed were not the most efficient way to perform this observation. Each stellar mode frame effectively incurs 8 s of overheads due to data transfer from the instrument to the spacecraft. As our observations only required the data in the field of view with the star, it was possible to save both data volume by collecting data in only two channels and with a cadence of 4 s. Consequently, we designed a special engineering template [Instrument Engineering Request (IER)] to optimize the observations. IERs have been used successfully in other planet transit experiments (Charbonneau et al. 2005), and they can typically double the efficiency, and our IER enabled us to reduce the total required observing time for all four channels to only 13.4 h.

2.2 Data reduction and flux measurements

We used the flat-fielded, cosmic-ray-corrected and flux-calibrated data files provided by the *Spitzer* pipeline. Each channel has been treated separately. We measured the flux of the target on each image using the version 2.5.0 of the SEXTRACTOR package (Bertin & Arnouts 1996), with a standard set of parameters for *Spitzer* (Infrared Array Camera Data Handbook 2006). The centroid determination was achieved with point spread function (PSF) fitting. We performed both aperture photometry, and PSF fitting photometry. In Fig. 1, for all the six observed transits, we give the raw magnitude measurements (normalized using the post-transit observation), the variation of the centroid in *X*- and *Y*-axes, and the distance of the centroid from the lower left-hand corner of the pixel (the pixel phase). A quick inspection shows that all observations contain correlated noise of different nature, as expected when using the IRAC camera. We discuss this phenomenon, and how we corrected for it, channel by channel, in the next section.
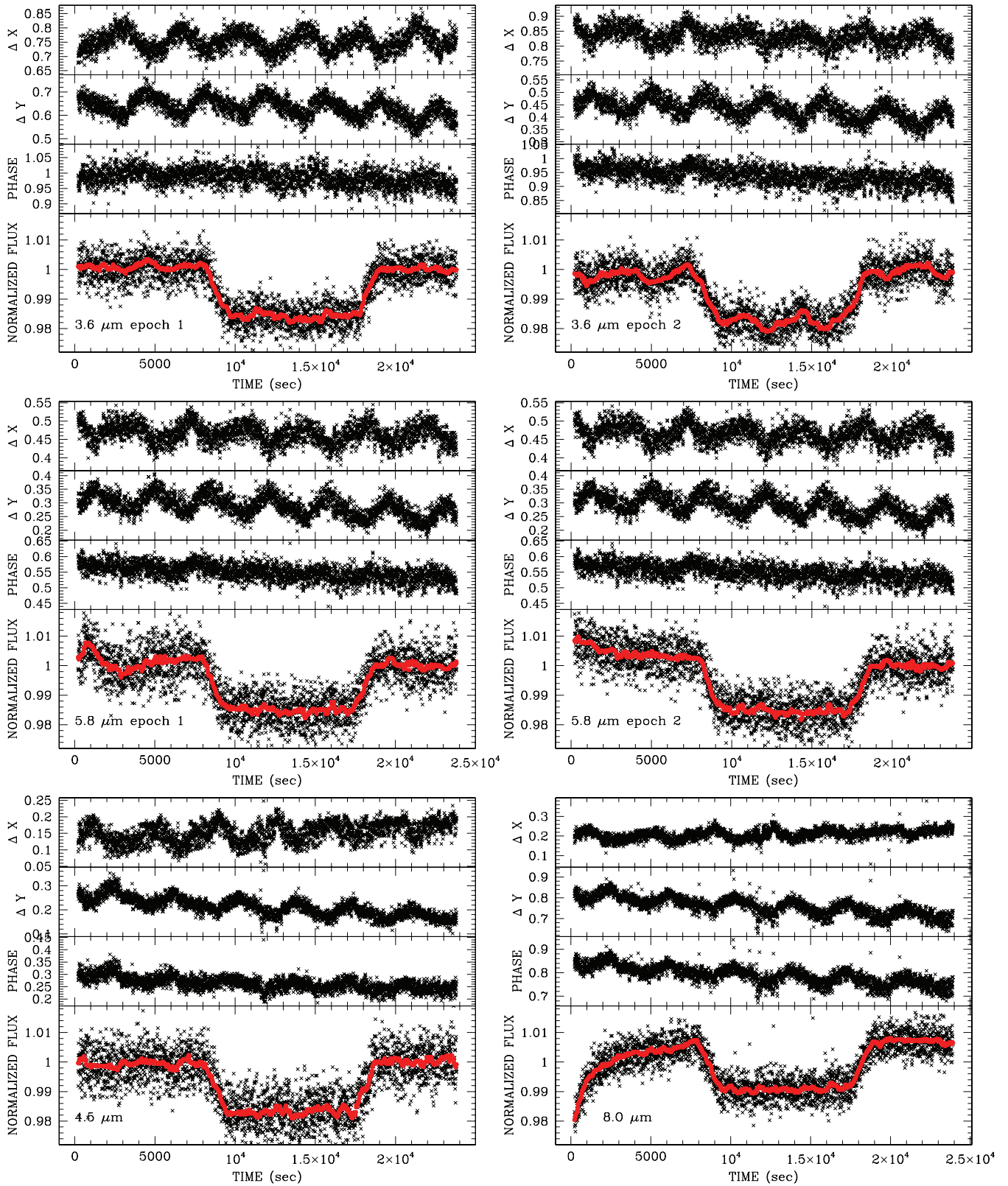
Figure 1. Raw photometric data for 3.6 μm (epochs 1 and 2), 5.8 μm (epochs 1 and 2), 4.5 μm and 8 μm obtained with IRAC. Each subpanel has the same structure showing from top to bottom the variation of the centroid position in X, Y, and lastly the distance of the centroid from the lower left-hand corner in the pixel (called the pixel phase, which can also be seen as the pointing error temporal amplitude). The lowest panel of each plot is the primary transit, and overplotted the 50-point median-stack smoothing. They provide a synoptic view of the systematic trends present in IRAC primary transit data.

3 ESTIMATION AND ATTENUATION OF CORRELATED NOISE

3.1 Correcting the pixel phase effects

It has been well established that the IRAC channels exhibit pixel phase effects due to a combination of non-uniform response function within each pixel and very small pointing variations (Morales-Calderón et al. 2006; Beaulieu et al. 2008). These effects are most prominent within the 3.6- and 4.5-μm photometry and to a lesser degree in the other two channels. We note that previous studies have not corrected for possible pixel phase effects at 5.8 or 8 μm, but in this paper we evaluate the effectiveness of implementing it in all channels. Table 1 shows the noise properties and effects of pixel-phase-effect attenuation on each IRAC channel.

Pixel-phase information is retrieved by using SExtractor's PSF fitting to obtain estimates of the X and Y pixel-phase for each exposure. In contrast, the flux for each exposure is obtained through aperture photometry since this offers substantially larger signal-to-noise ratio compared to the PSF flux estimates.

A typical procedure is to directly correlate the X and Y phases to the out-of-transit fluxes to some kind of four- or five-parameter fit (Morales-Calderón et al. 2006; Beaulieu et al. 2008; Knutson et al. 2008) and in this paper we will adopt a similar approach. We note that the PSF-fitted estimates of X and Y exhibit significant scatter at the same level as the amplitude of the periodic variations in each. This scatter is caused predominantly by photon noise slightly distorting the PSF shape in a random manner and thus causing the fitting algorithm to deviate from the true value. The pixel phase effect is physically induced by the spacecraft motion and so we only wish to correlate to this property, as opposed to the random photon-noise-induced scatter of X and Y. In order to do this, we fit a smooth function through the pixel-variations themselves before attempting to correlate to the out-of-transit flux.

Our analysis of the X and Y phases reveals a dominant ~1 h period sinusoidal-like variation in X and Y, characteristic of small elliptical motion in *Spitzer*'s pointing, with a more complex time-trend overlaid. For each channel, we apply a non-linear regression of a sinusoidal wave to the phases, in order to determine the best-fitting dominant period, P_{phase} (typically close to 1 h). We then calculate the median of the phases from the ith data point to the jth, where $t_j = t_i + P_{\text{phase}}$, (where t_k is the time-stamp of the kth exposure) and repeat from $i = 1$ up to the end of the data list. This moving-window-function essentially purges the dominant period from the phases and thus allows us to obtain a robust determination of the second-order phase variations, which may then be fitted for using a polynomial, of orders varying from 2 to 4 depending on the degree of curvature in the resultant phase trends.

We have now calculated the function which describes the pixel phase variation of X and Y with respect to time, as induced by spacecraft motion. This function is then correlated to the actual out-of-transit photometry to find a fit to the function $a + bX(t) + cY(t) + d[X(t)]^2 + e[Y(t)]^2$. We find including an additional cross-term does not further improve the pixel-phase-effect attenuation.

For 3.6 μm (epochs 1 and 2) and 4.5 μm, we removed pixel-phase effects of rms amplitude 0.49, 1.51 and 0.57 mmag, respectively, over the standard 8.4-s cadence. The second epoch at 3.6 μm, is particularly polluted by pixel phase response, possibly due to a large inhomogeneity in response close to the PSF centroid position (pixels 131, 128 of the detector). Repeating the process for the remaining channels (after the other systematic effects were removed first, see next sections for details), we are able to remove 0.29 and 0.24 mmag for 5.8 μm (epoch 2) and 8 μm, respectively. Thus the pixel-phase-induced variations are half of the minimum variations founds at 3.6 and 4.5 μm.

3.2 Correcting systematic trends at 5.8 μm

In the exoplanet community, at least two different methods have been proposed to correct for the systematic effects observed at 5.8 μm, characterized by a large change in flux near the commencement of the observations. One frequently adopted procedure adopted is to discard the first ~30 min of observations (Charbonneau et al. 2008; Knutson et al. 2008) and then detrend the remaining data. For example, in the case of HD 189733b primary transit observations, Beaulieu et al. (2008) removed the first 20 min, and then applied a linear correction. Another method proposed by Désert et al. (2009) involves not excluding these first 20 min but attempt to correct the data using a logarithmic parametrization (see Section 4.4): $a + bt + c\log(t - t_0) + d[\log(t - t_0)]^2$. Employing different corrective procedures will undoubtedly yield significantly different transit parameters and so we must carefully consider the effect of each proposed correction.

The most intuitive starting point is a visual inspection of the flux time-series for our two measurements at 5.8 μm. In Fig. 2, we exclude the transit event and show the behaviour of the out-of-transit flux (the baseline) with an overlaid 50-point median smoothing as a visual guide. The first epoch exhibits a clear discontinuity between the photometry in the region $0 \leq t \lesssim 5500$ s and the subsequent data. The behaviour of this initial photometry does not match a 'linear drift, a 'ramp' style effect or any commonly employed analytic form. The origin of the observed behaviour is unclear and is present in many different trial aperture sizes, between 2.5 and 20 pixels radius, suggesting an instrumental effect located either very close to the centroid position or globally across the detector array.

Repeating the visual inspection for the second epoch, we observe a less pronounced version of this behaviour in the region $0 \leq t \lesssim 2800$ s (note that this behaviour is not seen in any other channels). However, the effect is ostensibly sufficiently small that we cannot

Table 1. Noise properties and effects of pixel-phase-effect attenuation on each IRAC channel.

|	3.6 μm (epoch 1)	3.6 μm (epoch 2)	4.5 μm	8.0 μm	5.8 μm (epoch 2)	5.8 μm (epoch 1)
Before correction						
Baseline rms (mmag)	3.560 05	3.8848	4.930 71	3.266 71	4.313 89	4.820 04
In per cent above photon noise	75.5011	92.3528	119.734	79.3238	57.5393	76.1831
After correction						
Baseline rms (mmag)	3.526 21	3.577 96	4.8974	3.258 21	4.3042	4.7886
In per cent above photon noise	73.8329	77.1596	118.249	78.8573	57.1856	75.0341
Noise removed (mmag)	0.489 685	1.513 25	0.572 162	0.235 493	0.288 931	0.549 594

8
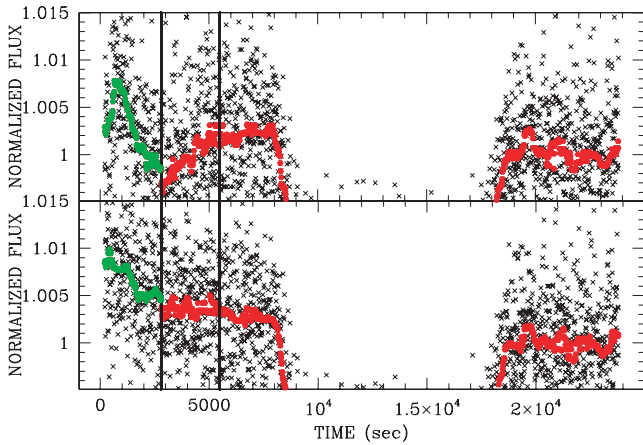
Figure 2. Zoom on the IRAC 5.8-μm observations to show the systematic trends that are present (first and second epochs in the upper and lower panels, respectively). We show the data and the 50-point median-stack smoothing. For the second epoch note the change of behaviour around 2800 s, indicated by the vertical line. Note that the behaviour after 2800 s is different between the two epochs.

Figure 3. Local gradient of each time-stamp from the raw flux measurements obtained with IRAC at 5.8 μm for the two epochs of HD 209458b and HD 189733b. Note that the three exhibit similar behaviour for the first 2000 s. The first epoch for HD 209458b has a larger amplitude of systematics, but the second epoch of HD 209458b and the observation of HD 189733b have remarkably similar behaviours.

claim it is the same behaviour from a visual inspection of the time-series alone. Therefore, we require a more in-depth analysis to provide a conclusion as to whether the systematic behaviours in epoch 1 and epoch 2 are the same. In order to understand what kind of analysis this should be, we need to explicitly qualify the question we are trying to answer.

The difference between the truncation + linear trend versus the logarithmic correction can be summarized by one key point: the former proposes that the initial data are incoherent with the latter data and cannot be characterized by a smooth analytic function. The latter works under the hypothesis that the entire time-series is following one single smooth analytic description. We therefore wish to understand whether the properties of a smooth analytic function are consistent with the properties of the observed time-series. This is the critical question which we must answer.

One key property of the smooth analytic, logarithmic function proposed by Désert et al. (2009) is that the differential of the function with respect time provides another smooth analytic function. In contrast, the truncation + linear trend hypothesis postulates that since the initial data exhibit discontinuous behaviour, then the differential of this must also be discontinuous. So taking the differential of the time-series will clearly resolve which hypothesis has the most supporting evidence.

To achieve this goal, we first extract the uncorrected out-of-transit fluxes only and remove outliers for both epoch 2 and epoch 1 using a median absolute deviation analysis. We then create a moving 150-point window, in which we calculate the local gradient at each point. We do this by subtracting the median of the time-stamps from each time-stamp within a given window (to move the pivot along) and then performing a weighted linear regression. We define the weights as the square of the reciprocal of each flux measurement. In addition to the HD 209458b data presented here, we perform the same process on the HD 189733b 5.8-μm data (used in Tinetti et al. 2007; Beaulieu et al. 2008; Désert et al. 2009) for comparison giving us three data sets. Errors for each gradient stamp are computed using the weighted linear regression algorithm.

In Fig. 3, we see all three local gradients plotted together. Ostensibly, there seems to be strong correlations between the three measurements, despite one of them being for a completely different
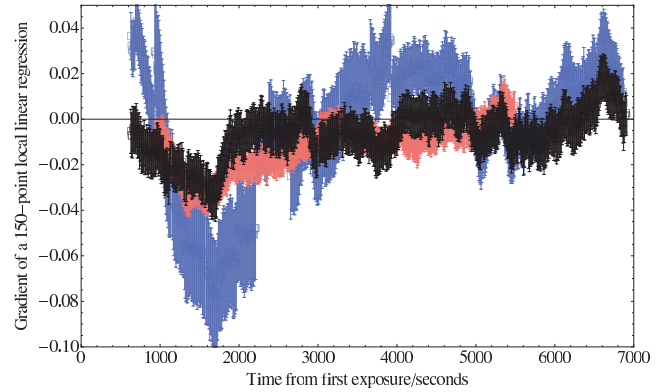
star. In particular, there is a strong dip at around 2000 s after the first exposure in all three observations. In Fig. 4, we plot just the epoch 2 of HD 209458 and also overlay the local gradients obtained from a logarithmic fit of the baseline (equivalent to the first differential of this function with respect to time). It is clear that the logarithmic fit cannot explain the strong negative peak observed in the gradients data. Furthermore, the clear presence of discontinuous behaviour in the local gradients supports the hypothesis that no continuous analytic function can correct this behaviour.

Although the three measurements appear correlated, we may quantify these correlations. Comparing any two channels, we define one as the reference data and one as the comparison data. We first ensure the minimum to maximum time-stamps of both sets are the same by clipping the longer set appropriately. We then perform a linear interpolation of both the gradient measurements and the uncertainties, for the comparison data. This allows us to accurately estimate the gradient values at like-for-like time-stamps. Regenerating the comparison gradients data using the interpolation function, we evaluate the correlation between the two using Pearson's correlation coefficient. We repeat the same process for randomly generated data with the same uncertainties and array length as the original.
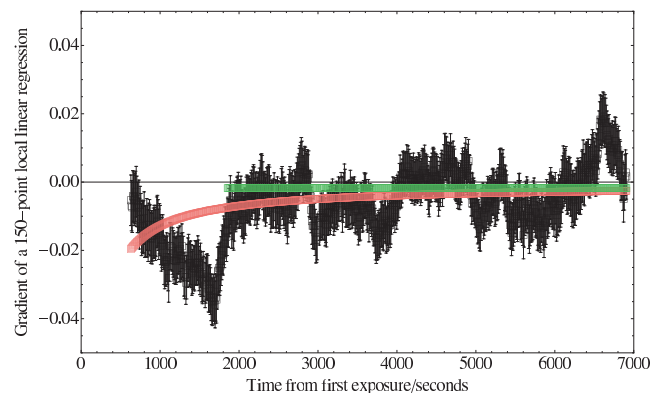

Figure 4. Local gradient of each time-stamp from the raw flux measurements obtained with IRAC 5.8 μm (epoch 2), computed using a linear regression of a moving 150-point window. Black indicates the observed local gradients, which differ greatly from those obtained using a logarithmic fit of the photometry (red). Note the 1600 s peak/discontinuity.

This is repeated 100 000 times in order to estimate the expected correlations from random noise.

Although they have been taken more than 7 months apart, we find epoch 1 and epoch 2 for HD 209458 have correlation Corr (209458epoch2, 209458epoch1) = 0.678. The 10^5 randomly generated noise values yield 0.001 ± 0.037. This makes the correlation significant at the 18.4σ level. Repeating the exercise for epoch 2 of HD 209458 and for the observations of HD 189733b (taken 3 yr apart), we have Corr(209458epoch2, 189733) = 0.658. The randomly generated noise yields 0.002 ± 0.043, making the observed correlation significant at the 15.2σ level. In conclusion, the correlations in the local gradient plots are highly significant even for observations separated by years on different stars. We therefore conclude the observed behaviour must be instrumental effects for 5.8-μm detector array itself.

The largest feature is that of the 'negative spike' at around 2000 s. After this, all three observations exhibit variations consistent with that of a singular constant value, i.e. a linear fit. The reduced χ^2 of these three channels may be computed both for all data and for those data after the negative spike. We find the values always decrease by excluding the negative spike; quantitatively we have respective changes of $1.18 \rightarrow 0.58$ for HD 209458 epoch 2, $2.99 \rightarrow 1.24$ for HD 209458 epoch 1 and $2.66 \rightarrow 1.51$ for HD 189733. Therefore we can see that the instrumental systematic effects of 5.8 μm can be split into two regimes, pre- and post-spike. The pre-spike data exhibit discontinuous behaviour compared to the latter data and cannot be characterized by a smooth continuous function. The post-data conform to a linear fit.

We therefore conclude that an analysis of the differential of the time-series supports the hypothesis that the 5.8-μm correction should be to remove the discontinuous data before the gradient spike and then use a linear fit for the remainder. It would therefore seem that at 5.8 μm the detector requires a certain amount of time to settle into a stable regime, as indicated also in earlier studies (Beaulieu et al. 2008; Charbonneau et al. 2008; Knutson et al. 2008).

Despite the evidence from this gradients analysis, we may conceive of several other possible tests to be certain that the logarithmic correction not favoured by the data. Using the light-curve fitting code described in Section 4.3, we fitted two possible systematic correction light curve: (1) a truncation of the first 2800 s, followed by a linear fit to the remaining baseline data (e.g. Beaulieu et al. 2007; Harrington et al. 2007; Knutson et al. 2007) and (2) a logarithmic fit to all baseline data (e.g. Désert et al. 2009). We select several properties to compare these two possible corrections.

(i) Adopting a baseline within $2814 \leq t \leq 7543$ s (i.e. after the discontinuous behaviour) and $19\,605 \leq t \leq 23\,974$ s, constituting 1082 data points, we compute the χ^2 for both the linear and the logarithmic fit. Despite using two extra free parameters, the logarithmic produces a larger $\chi^2 = 1358.1$ compared to a linear fit with $\chi^2 = 1338.7$ (flux uncertainties based on photon noise only).

(ii) We may also compare the χ^2 of the entire light-curve fit (using the model described in Section 4.3). In this case, we must scale the χ^2 for a fair comparison since the linear fit uses fewer points due to the truncation procedure. Comparing the reduced χ^2 between the two corrections we find lower values for the linear fit again – 1.045 versus 1.014 or 1.031 versus 1.000, depending whether we additionally correct for pixel phase.[1]

(iii) We use the fitted transit duration, T, defined by Carter et al. (2009) which was shown to be highly robust and non-degenerate. T is expected to be independent of wavelength as the only possible parameter which could vary is R_* which is not expected to exhibit significant changes between different wavelengths. We therefore refit the Brown et al. (2001) *Hubble Space Telescope* (*HST*) light curve of HD 209458b, taken in the visible, with the same model used here. We find a transit duration of 9525^{+16}_{-14} s. In comparison, correcting the second epoch at 5.8 μm with a linear fit yields $T_{\rm lin} = 9518^{+50}_{-55}$ s and with a logarithmic fit $T_{\rm log} = 9546^{+51}_{-55}$ s.

(iv) In Fig. 4, the local gradients, as taken in 150-point bins, is compared to that expected from the logarithmic fit of the data. There is a very strong discrepancy between the data and the model before 2000 s.

Thus, we find employing a logarithmic fit, with two additional free parameters, cannot be shown to offer any kind of improvement over the linear fit. The gradient analysis presented above shows that the logarithmic parametrization is not adapted. Moreover, it is disfavoured by $\Delta\chi^2 = 20$. Since every single test performed has supported the truncation and linear trend correction, this method will be adopted as the preferred corrective procedure in our subsequent analysis.

3.3 Correcting the ramp at 8 μm

The ramp effect at 8 μm is well documented and so too is the methodology for correcting this phenomenon (Agol et al. 2008, and references therein). Unlike the 5.8-μm data, there are no known discontinuities in the time-series and thus the correction may be achieved using a smooth analytic function. We fit a time-trend to the out-of-transit data of the form $a+bt+c\log(t-t_0) +d[\log(t-t_0)]^2$ where t_0 is chosen to be 30 s before the observations begin to prevent the function exploding at $t = 0$.

4 FITTING THE TRANSIT LIGHT CURVES

Among the six transit light curves, we have four of high quality with well understood and corrected systematic effects: the first epoch at 3.6, 4.5 μm, the second epoch at 5.8 and 8 μm. The second epoch at 3.6 μm and the first epoch at 5.8 μm will be treated separately. The final light curves, best-fitting model and residuals are shown in Fig. 5.

4.1 Limb darkening

Accurate limb-darkening coefficients were calculated for each of the four IRAC bands. We adopted the following stellar properties: $T_{\rm eff} = 6100$ K, $\log g = 4.38$ and [Fe/H] = 0. We employed the Kurucz (2006) atmosphere model data base providing intensities at 17 emergent angles, which we interpolated linearly at the adopted $T_{\rm eff}$ and $\log g$ values. The passband-convolved intensities at each of the emergent angles were calculated following the procedure in Claret (2000). To compute the coefficients we considered the following expression:

$$\frac{I(\mu)}{I(1)} = 1 - \sum_{k=1}^{4} c_k(1 - \mu^{k/2}),$$

where I is the intensity, μ is the cosine of the emergent angle and c_k are the coefficients. The final coefficients resulted from a least squares singular value decomposition fit to 11 of the 17 available emergent angles. The reason to eliminate six of the angles is avoiding excessive weight on the stellar limb by using a uniform sampling

---

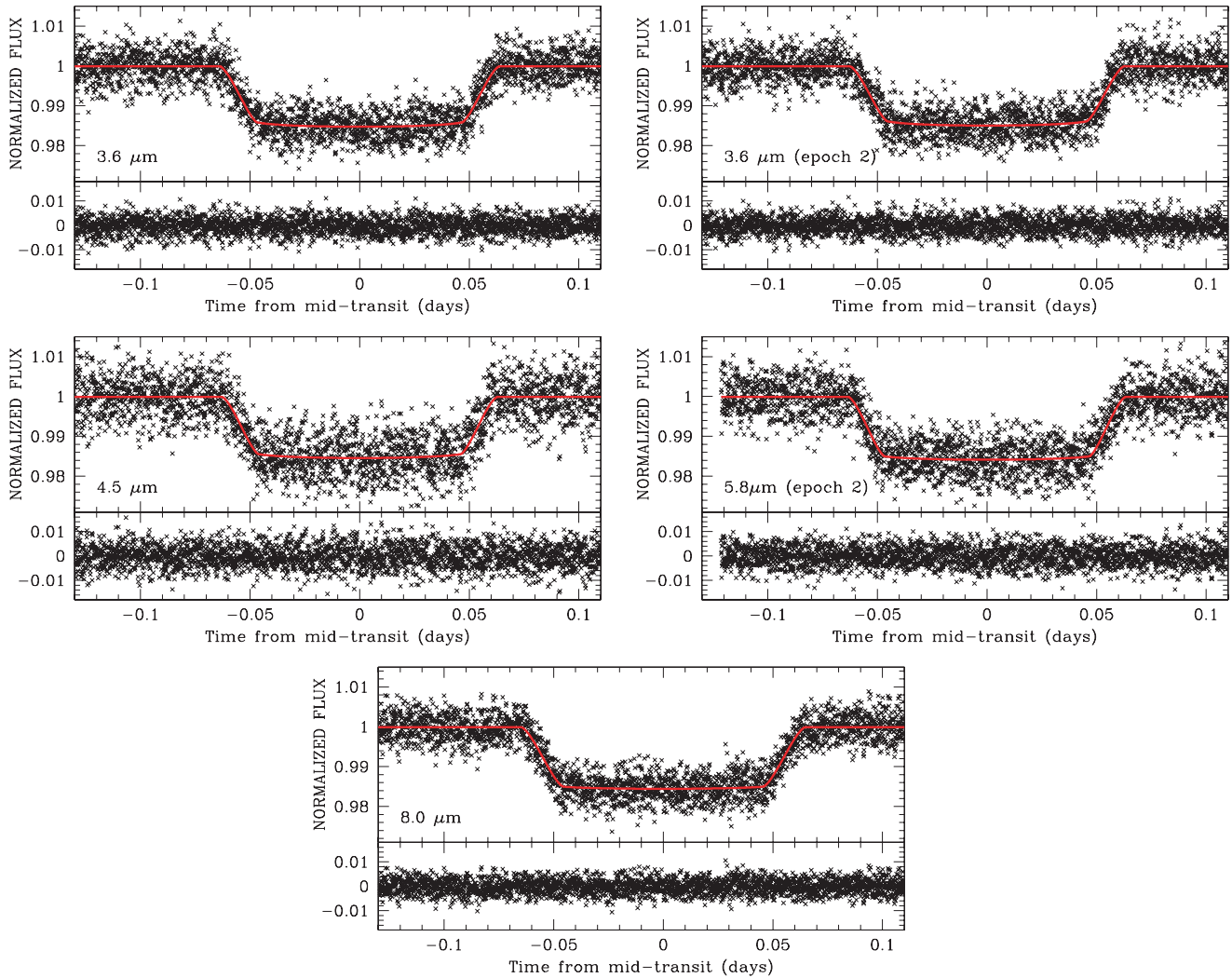[1]Reduced χ^2 values have been rescaled so that lowest value is equal to unity.

Figure 5. Final light curves, best-fitting model and residuals at 3.6 μm (epochs 1 and 2), 4.5 μm, 5.8 μm (epoch 2) and 8 μm. In the residuals subpanel we will overplot the 50-point median-stack smoothing of the residuals.

Table 2. Limb-darkening coefficients.

Channel	c1	c2	c3	c4
3.6 μm	0.267 0569	0.139 6675	−0.190 0802	0.064 018
4.5 μm	0.332 5055	−0.199 9922	0.185 8255	−0.070 3259
5.8 μm	0.326 9256	−0.271 5499	0.225 8883	−0.068 4003
8 μm	0.280 0222	−0.227 8080	0.145 1840	−0.027 3881

(10 μ values from 0.1 to 1, plus $\mu = 0.05$), as suggested by Díaz-Cordovés, Claret & Giménez (1995). The coefficients are given in Table 2.

4.2 Markov Chain Monte Carlo fit to the data

We adopt the physical model of a transit light curve through the expressions of Mandel & Agol (2002) and orbital eccentricity using the equations of Kipping (2008). We sampled the parameter space with Markov Chain Monte Carlo (MCMC) codes (Doran & Muller 2004) originally developed for microlensing (Dong et al. 2008; Batista et al. 2009) and adapted to fit transit data. We first made an independent fit for 3.6 μm (epochs 1 and 2), 4.5, 5.8 μm (epoch 2) and 8 μm. We adopted a fixed value of period to be $P = 3.524\,749$ d (Knutson et al. 2007). For each channel, five parameters are fitted, namely the out-of-transit baseline, the orbital inclination i, the ratio between the orbital semimajor axis and the stellar radius a/R_*, the ratio of radii k and the mid-time transit t_c. We also permit the orbital eccentricity e and the position of periastron ω to move in a restricted range, corresponding to the best-fitting values derived by Winn et al. (2005) including their error bars. The five other parameters are free. The error bars of the data have been rescaled to make the χ^2 per degree of freedom equal to unity. The results are shown in Table 3.

As some physical parameters should be the same for all bands, we made a simultaneous fit to the best observations, namely 3.6 μm (epoch 1), 4.5, 5.8 μm (epoch 2) and 8 μm, in which four parameters are shared by all channels: P, e, i, ω and a/R_*. Three other parameters, k, t_c and the baseline, are fitted independently for each band and are allowed to move within the range obtained in the individual fits. We decided to fit separately 3.6 μm (epoch 2), forcing the four shared parameters to be equal to the values derived from the best fit with the four other channels. The results are shown in Table 4.

Table 3. Markov Chain Monte Carlo fit to individual primary transits observed by IRAC. We list all the fitted parameters (see the text for the description), and in particular the ratio of radii $k = R_p/R_*$, the orbital semimajor axis divided by the stellar radius, a/R_*, the orbital inclination, i and the mid-transit time, t_c.

	3.6 µm (epoch 1)	3.6 µm (epoch 2)	4.5 µm	5.8 µm (epoch 2)	8 µm
i (°)	87.00 ± 0.11	86.67 ± 0.15	86.87 ± 0.10	86.84 ± 0.11	86.37 ± 0.13
A/R_*	8.89 ± 0.06	8.84 ± 0.10	8.91 ± 0.05	8.84 ± 0.07	8.49 ± 0.08
$k = R_p/R_*$	$0.120\,835 \pm 0.000\,54$	$0.120\,387 \pm 0.000\,53$	$0.1218 \pm 0.000\,72$	$0.1244 \pm 0.000\,59$	$0.1240 \pm 0.000\,46$
$k^2 = (R_p/R_*)^2$	1.460 ± 0.013 per cent	1.449 ± 0.013 per cent	1.4835 ± 0.017 per cent	1.547 ± 0.015 per cent	1.538 ± 0.011 per cent

Table 4. Markov Chain Monte Carlo fit to IRAC data. The first column shows a join fit to the best four band observations, namely 3.6 µm (epoch 1), 4.5, 5.8 µm (epoch 2) and 8 µm. Then we impose the parameters $i, A/R_*, e, \omega$ and fit the ratio of the radii k and the mid-transit time t_c for the second epoch at 3.6 µm and the first epoch at 5.8 µm.

	3.6 µm (epoch 1) + 4.5 µm + 5.8 µm (epoch 2) + 8 µm	(3.6 µm) epoch 2	(5.8 µm) epoch 1
i (°)	86.76 ± 0.10		
a/R_*	8.77 ± 0.07		
$k = (R_p/R_*)$			
3.6 µm	$0.121\,215 \pm 0.000\,54$	$0.120\,343 \pm 0.000\,53$	
4.5 µm	$0.121\,568 \pm 0.000\,72$		
5.8 µm	$0.1244 \pm 0.000\,59$		$0.1246 \pm 0.000\,95$
8 µm	$0.123\,90 \pm 0.000\,46$		
$k^2 = (R_p/R_*)^2$			
3.6 µm	1.469 ± 0.013 per cent	1.448 ± 0.013 per cent	
4.5 µm	1.478 ± 0.017 per cent		
5.8 µm	1.549 ± 0.015 per cent		1.552 ± 0.032 per cent
8.0 µm	1.535 ± 0.011 per cent		

4.3 Prayer-bead Monte Carlo fit to the data

We also fitted all the transit data with the code used by Fossey, Waldmann & Kipping (2009), incorporating the effects of non-linear limb darkening through the expressions of Mandel & Agol (2002) and orbital eccentricity using the equations of Kipping (2008). We fixed the orbital eccentricity e and position of periastron ϖ to the best-fitting values derived by Winn et al. (2005), and adjusted $k, a/R_*, b$ and t_c to find a minimum in χ^2. Although the parameters a/R_* and b show a degree of covariance, Carter et al. (2008) have shown that the transit duration T, ratio of radii k and mid-transit time t_c are non-degenerate parameters; these parameters are also less affected by systematic errors in orbital eccentricity and thus can be taken to be more reliably constrained than $a/R_*, b$ or the inclination i.

We use the genetic algorithm PIKAIA (see Metcalfe & Charbonneau 2003) to find an initial, approximate solution, which is used as the starting point for a χ^2-minimization using the downhill-simplex AMOEBA algorithm (Press et al. 1992). The initial best-fitting parameters from AMOEBA are randomly perturbed by up to 40 per cent of their value and refitted in 100 trials to check the robustness of the best-fitting solution.

To obtain the final parameter uncertainties, we employ a 'prayer-bead' Monte Carlo simulation of the unbinned data, as used by Gillon et al. (2007). Here, the set of residuals from the best-fitting solution is shifted by one data point and added to the best-fitting transit model to generate a new data set, with the residual at the end of the data series wrapping around to the beginning. The new data set is refitted, and the process repeated until the set of residuals has been cycled through the entire data series. This procedure has the advantage of preserving the structure of any residual correlated noise within the light curve in each simulation. For the unbinned

data we then have typically 2500–3000 samples from which the parameter uncertainties may be estimated, which we take to be the values comprising 68.3 per cent of the sample about the median of each parameter distribution. The median and uncertainties are compared to the fitted value in each case, to check the robustness of the simulations and to assign upper and lower limits on the parameters. In all cases, we found the difference between the median and the best-fitting parameter was insignificant.

Table 5 lists the fitted depth, ratio of radii k, transit duration T, orbital inclination i and a/R_* from this fitting procedure, for each of the transits.

4.4 The case of the epoch 1 of 5.8 µm

The first epoch of 5.8 µm requires special consideration due to the extremely pronounced nature of the systematic errors for this data set. In Section 3.2 we demonstrated that the corrective procedure most consistent with the observational evidence is to the truncate the initial data exhibiting discontinuous behaviour and then perform a linear correction through the remaining baseline data. Since the systematic effect is so pronounced here, we took a conservative approach by assuming the systematic may persist up the moment of mid-transit. We therefore exclude all data before the mid-transit and adopt the physical parameters $(i, a/R_*)$ derived from the global MCMC fit and reported in Table 4, and fitted the baseline, the ratio of radii k and the mid-transit time t_c.

In Fig. 6 we compare epoch 1 data and the model fitted on the data from the mid-transit. Inspection of the residuals after the mid-transit indicates a good fit to the data. The data from the first half of the observations show the uncorrected systematic trends at work. It is clear that they are of different nature from the one of epoch 2. We add the measured ratio of radii and depth in the last

Table 5. Best-fitting transit depths, ratio of radii k, duration T, orbital semimajor axis divided by the stellar radius a/R_*, inclination i, mid-transit time t_c found using the prayer-bead Monte Carlo fit method described in Section 4.1.

Band (μm)	$k^2 = (R_p/R_*)^2$	$k = R_p/R_*$	T (s)	a/R_*	i
3.6 (epoch 1)	$1.462^{+0.011}_{-0.012}$	$0.12089^{+0.00045}_{-0.00048}$	9581^{+57}_{-47}	8.88 ± 0.02	86.99 ± 0.18
4.5	$1.482^{+0.014}_{-0.014}$	$0.12174^{+0.00056}_{-0.00056}$	9437^{+60}_{-51}	9.09 ± 0.01	87.15 ± 0.10
8.0	$1.538^{+0.011}_{-0.011}$	$0.12403^{+0.00043}_{-0.00045}$	9580^{+58}_{-49}	8.50 ± 0.02	86.32 ± 0.20
3.6 (epoch 2)	$1.449^{+0.010}_{-0.010}$	$0.12038^{+0.00043}_{-0.00043}$	9358^{+57}_{-48}	8.86 ± 0.02	86.70 ± 0.13
5.8 (epoch 2)	$1.542^{+0.0099}_{-0.0096}$	$0.12416^{+0.00040}_{-0.00039}$	9517^{+50}_{-54}	9.13 ± 0.01	87.22 ± 0.12
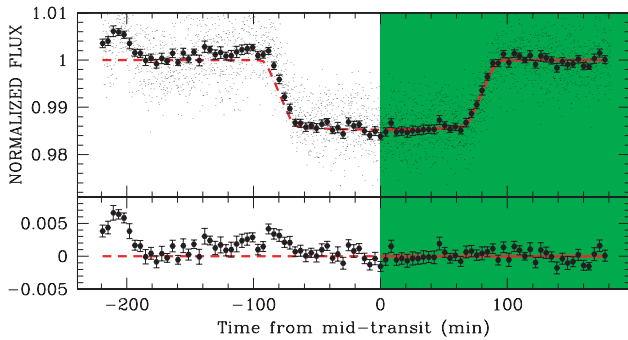
Figure 6. The uncorrected unbinned and binned (30 points) data from first epoch at 5.8 μm and the underlined model computed for the second epoch (corrected for systematics). The lower panel shows the residuals of the binned data (unbinned data omitted for clarity). The shaded area is marking the second half of the transit and the post transit observations used in the fit.

column of Table 4, and last row of Table 5. The results we therefore obtain from second epoch are consistent with the first epoch.

As a final check of the procedure, we decided to treat also the second epoch at 5.8 μm the same way. We take the uncorrected data, exclude the first half of the data up to the mid-transit, and fit the light curve. We report the measured depth by this procedure to be 1.540 ± 0.029 per cent. It is perfectly compatible with our complete fits reported in Tables 3–5.

4.5 Sanity check: grid calculations

As a check on our methodology we imposed the physical parameters derived from Knutson et al. (2008) in the approximation of circular orbit, and fitted for the baselines, ratio of radii k and mid-time transit t_c, using a simple χ^2 minimization. This gradient based method explores the local minimum around the physical solution found by Knutson et al. (2008). By comparing the results to the ones obtained with the Monte Carlo methods, we found that the transit depths agree well within the error bars. By contrast the other parameters (inclination, a/R_*) are highly degenerate.

4.6 Influence of spots

An effect to consider when comparing transit depth at different wavelengths is the influence of stellar surface inhomogeneities, i.e., star-spots. Depending on the spot distribution, the occulted stellar area during the transit can be brighter or dimmer than the average photosphere. In the case of HD 189733, a moderately active star with visible photometric variations of ∼3 per cent (peak to peak), the differential effect in the IRAC 3.6- and 5.8-μm bands was evaluated by Beaulieu et al. (2008) to be below 0.01 per cent. HD 209458 is a chromospherically inactive star with an estimated age close to

that of the Sun (e.g. Mazeh et al. 2000; Cody & Sasselov 2002; Torres, Winn & Holman 2008). It is thus reasonable to assume a level of photometric variations similar to that of the Sun, i.e. 0.2–0.3 per cent peak to peak (Fröhlich & Lean 2004). Scaling the calculations carried out for HD 189733, the expected differential effect of star-spots on the IRAC bands for HD 209458 is likely to be 10–20 times smaller, and therefore well below 0.001 per cent. Our calculations show that star-spots have negligible influence when compared with our measurement uncertainties (∼0.011–0.017 per cent); see Tables 3, 4 and 5.

4.7 Comments about different epochs at 3.6 and 5.8 μm

We asked for two epochs for HD 209458b at 3.6 and 5.8 μm with the prime intention of demonstrating the possibility of co-adding multiple epoch observations, and/or to be able to check for the variability in the system. The two epochs are separated by 7 months, and the observing setups are identical.

First, at 3.6 μm the data are affected by systematic trends of the same nature due to the pixel scale effect. We note a factor of 3 in the amplitude of the systematic trends between the two epochs. We measure the two transit depth to be 1.469 ± 0.013 per cent and 1.448 ± 0.013 per cent, respectively. The results are compatible between the two channels.

Secondly, at 5.8 μm the situation is more complex. The second epoch showed the expected behaviour, and we have been able to correct for systematics, and to fit it. For the first epoch, we chose to discard the first half of the data, and fit the uncorrected remaining data set. We measure the two transit depth to be 1.552 ± 0.032 and 1.549 ± 0.015 per cent, respectively. The results are compatible between the two channels.

Even when centring on the same pixels of the detector, observing the same target several months apart, different systematics are at work. It is clear that the different data sets should be analysed for systematics and then corrected individually. Then, multiple epochs can be compared and/or added.

4.8 Results

We have chosen three approaches to fit the data, i.e. grid calculations with ephemeris from Knutson et al. 2008, MCMC and prayer-bead Monte Carlo. We obtain extremely similar results concerning the transit depth for the different wavelengths with the three techniques. The final results are listed in Table 4. As reported by Carter et al. (2008), there exists a degeneracy between the fitted orbital inclination i and a/R_*; whereas the ratio of radii k and the transit duration T are far more robust quantities. As a result of this robustness, we are able to use the fitted transit duration values as a test of whether the light curves appear physical or not.

From our six fitted light curves, the duration of 5.8 μm, epoch 1, cannot be used because only half the transit is fitted and so the fitted duration is dependent on priors. The other five light curves produce durations consistent with an average duration of $T = 9508 \pm 17$ s with a $\chi^2_{red} = 2.6$ suggesting an outlier. Removing the 3.6 μm, epoch 2, measurement to leave us just the four preferred observations we find $T = 9538 \pm 14$ s with $\chi^2_{red} = 1.1$. Since 3.6 μm, epoch 2, produces an outlier duration and is also known to exhibit by far the strongest pixel phase effect out of all of the observed light curves, we give it zero weighting in the later spectral analysis.

We find that our average durations are consistent with the duration we find when refitting the Brown et al. (2001) *HST* light curve of $T = 9525^{+16}_{-14}$ s. Consequently, we conclude that our results support a solution consistent with the Brown et al. (2001) observations and thus we may be confident that the systematic corrections have been successful.

4.9 Comparison with HD 189733b data

Beaulieu et al. (2008) gives an accurate description of the method adopted to analyse the two IRAC channels at 3.6 and 5.8 μm in the case of the hot Jupiter HD 189733b. The software BLUE (Alard, in preparation), was used to fit the PSF, as several stars were in the field and could be used as calibrators. One of the capabilities of BLUE is to provide optimized centroid estimates, and provide an accurate modelling of the PSF. In the case of HD 209458b one star only was present, so we had to adopt a different strategy, using the SEXTRACTOR program (Bertin and Arnouts 1996). The extracted light curves at 3.6 and 5.8 μm were corrected in a similar manner to that detailed in Beaulieu et al. (2008). In particular the 3.6-μm observations for the two planets show moderate or strong pixel-phase effects, that can be corrected for.

5.8-μm observations ostensibly represents the greatest challenge for correcting systematic errors as the behaviour is somewhat less understood than the 8.0-μm ramp and the pixel phase effects at 3.6 and 4.5 μm. This situation is exacerbated by the observation of a discontinuity in the photometry in two separate transit observations. At 5.8 μm there are no significant pixel-phase effects, but a linear drift with time, after the first 2800 s in the case of HD 209458b and 1800 s in the case of HD 189733b. For both planets we disregard the first 2800/1800 s and then simply apply a linear correction to the data after this point.

This is the main discrepancy between the Beaulieu et al. (2008) reduction and the one adopted by Désert et al. (2009). We do not discuss here previous results or methods adopted by the same team, incorporated in Ehrenreich et al. (2007), in part because we have already explained the reasons of their inadequacy in the Beaulieu et al. (2008), but most importantly as clearly abandoned by the authors themselves in the new version of the analysis of the same data provided by Désert et al. (2009). Désert et al. (2009) applied a logarithmic time-correlated detrending to this channel of the same form of 8.0-μm observations, but of opposite sign, i.e. an 'antiramp'. In contrast, we applied a truncation of the first 2800 s followed by a linear time-trend decorrelation.

The question as to which method is the correct one is naturally a topic of debate within the community but we believe we have produced here an in-depth analysis of each type of correction. In Section 3.2 we treated the 5.8-μm data with both methods and compared the resultant light curves. Several tests suggest that the truncation + linear detrending produces a more physical transit signal and an improved overall fit. In this paper, we acknowledge that there currently exists no widely accepted physical explanation
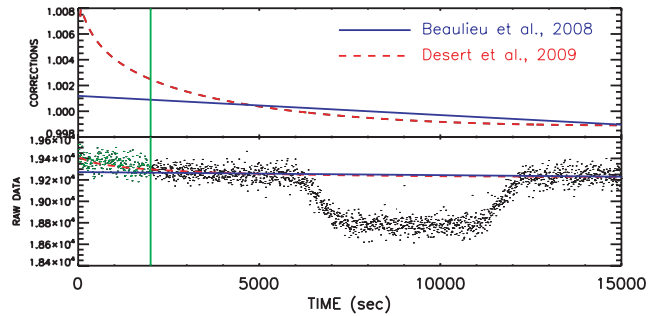

Figure 7. The lower panel shows the reprocessed HD 189733b data at 5.8 μm overplotted with the logarithmic correction from Désert et al. (2009) and the linear correction (Beaulieu et al. 2008). The vertical line indicates 2000 s. We provided in the text evidence to reject the first 2000 s. This figure shows how the logarithmic correction is overcorrecting in the transit.

Table 6. Comparison of values of transit depth for HD 189733b at 3.6 and 5.8 μm by Beaulieu et al. (2008), Ehrenreich et al. (2007) and Désert et al. (2009).

IRAC (μm)	Beaulieu 2008 (per cent)	Ehrenreich 2007 (per cent)	Désert 2009 (per cent)
3.6	2.383 ± 0.014	2.434 ± 0.026	2.387 ± 0.0093
5.8	2.457 ± 0.017	2.375 ± 0.04	2.393 ± 0.016

for the channel 3 systematic effects and thus the preference between the linear and logarithmic model must be made primarily on the basis of the light-curve information. On this basis, we cannot justify employing the logarithmic model over the method adopted here, given the range of evidence compiled.

Fig. 7 shows the reprocessed HD 189733b data at 5.8 μm overplotted with the logarithmic correction from Désert et al. (2009) and the linear correction (Beaulieu et al. 2008).

In our case, we find that adopting the logarithmic fit to our HD 209458 5.8-μm data would underestimate the transit depth by 0.035 per cent, generating a systematic error of $\sim 2.3\sigma$. We also estimate that the incorrect use of logarithmic correction leads to an underestimate of the transit depth of HD 189733 by 0.047 per cent, generating a systematic error of $\sim 2.9\sigma$. This accounts for the discrepancy between the studies of Désert et al. 2009 compared to Beaulieu et al. 2008. However, for case of 3.6 μm, both teams agree upon the corrective procedure, and so we should expect very similar results. Indeed, for the HD 189733 3.6-μm photometry, the values and error bars estimated by Beaulieu (2008) and Désert (2009) are in excellent agreement, as shown in Table 6.

5 DATA INTERPRETATION

To interpret the data, we used the radiative transfer models described in Tinetti et al. (2007a,b) and consider haze opacity, including its treatment in Griffith, Yelle & Marley (1998).

Our analysis includes the effects of water, methane, carbon dioxide, carbon monoxide, pressure-induced absorption of H_2–H_2. We do not consider the presence of particulates, because there is no indication of particles large enough (~ 3 μm) to affect the planet's mid-IR spectrum. The effects of water absorption are quantified with the BT2 water line list (Barber et al. 2006), which characterizes water absorption at the range of temperatures probed in HD 209458b. Methane was simulated by using a combination of HITRAN 2004 (Rothman et al. 2005) and PNNL data lists. Carbon monoxide
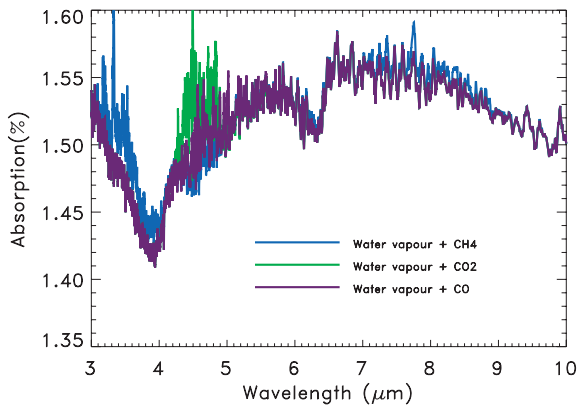
Figure 8. Simulated mid-IR spectra of the transiting hot Jupiter HD 209458b in the wavelength range 3–10 μm. Water absorption is responsible for the main pattern of the spectra. The additional presence of methane, CO and CO_2 are simulated in the blue, violet and green spectra, respectively.
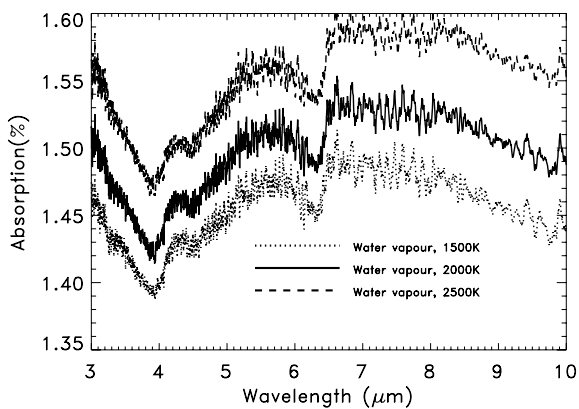

Figure 9. Modelled spectral absorptions of H_2O in the atmosphere of HD 209458b for 1500, 2000 and 2500 K.
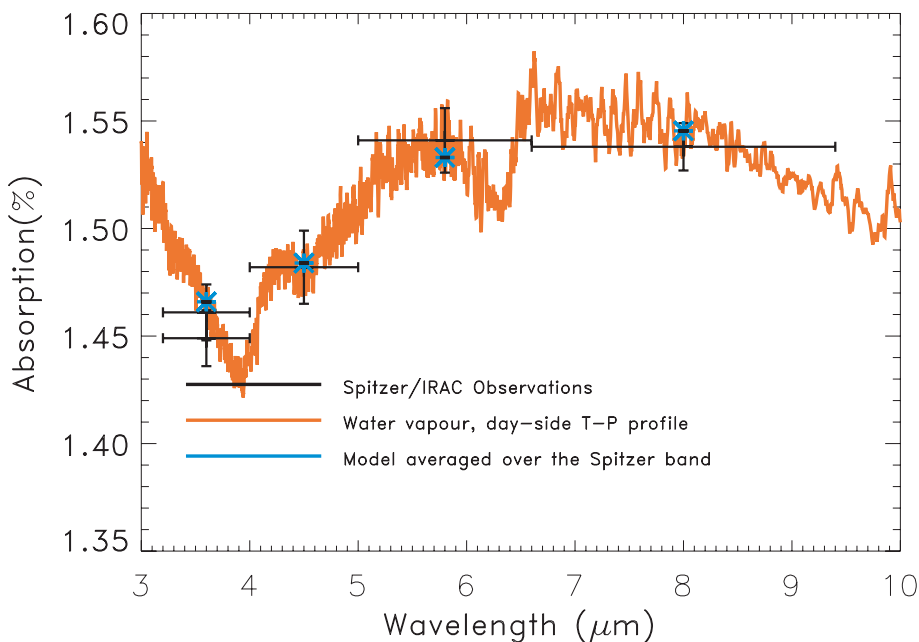
absorption coefficients were estimated with HITEMP (Rothman et al. 1995) whilst for carbon dioxide we employed a combination of HITEMP and CDSD-1000 (Carbon Dioxide Spectroscopic Databank version for high temperature applications; Tashkun & Perevalov 2008). The continuum was computed using H_2–H_2 absorption data (Borysow, Jorgensen & Fu 2001). In Fig. 8, we show the contribution of the different molecules combined to water.

The 3.6-μm (and to a lesser degree the one at 8 μm) IRAC channel measurement can be affected by the presence of methane. By contrast, CO_2 and CO may contribute in the passband at 4.5 μm.

We find absorption by water alone can explain the spectral characteristics of the photometric measurements, which probe pressure levels from 1 to 0.001 bars (Fig. 10). The determined water abundance depends on the assumed temperature profile and planetary radius. We find that the data can be interpreted, with a thermochemical equilibrium water abundance of 4.5×10^{-4} (Liang et al. 2003, 2004), assuming temperature profiles from Swain et al. 2009b. However, ~1 per cent difference in the estimate of the planetary radius, is compatible with water abundances 10 times smaller or larger, or with an overall change in the atmospheric temperature of about ~500 K (see Fig. 9). Additional primary transit data at different wavelengths are needed to improve the constraint.

While the contribution of other constituents is not necessary to interpret the measurements, mixing ratios of 10^{-7}, 10^{-6} and 10^{-4} of CO_2, CH_4 and CO, respectively, are allowed in our nominal model.

Spectroscopic data are needed to further investigate the composition of this planetary atmosphere.

6 CONCLUSION

We have presented here IRAC photometry data recording the primary transit of HD 209458b in four IR bands. We find that the systematics are very similar to those present in the data set obtained for the planet HD 189733b (Beaulieu et al. 2008), and therefore

Figure 10. Observations and spectral simulations of the atmosphere of HD 209458b. Black: *Spitzer* measurements where the horizontal bar is the IRAC bandwidth. Orange spectrum: water vapour and a thermal profile compatible with the day-side spectroscopy and photometry data (Swain et al. 2009b; Griffith & Tinetti, in preparation). Blue stars: simulated spectrum integrated over the *Spitzer* bands.

we adopted similar recipes to correct for them. We have performed MCMC and prayer-bead Monte Carlo fits to the data obtaining almost identical results. Our observations indicate the presence of water vapour in the atmosphere of HD 209458b, confirming previous detections of this molecule with different techniques/instruments. Interestingly, the thermal profiles derived for the day side are compatible with this set of data probing essentially the planetary terminator. It is possible that additional molecules, such as methane, CO and/or CO_2 are also present, but the lack of spectral resolution of our data have prevented these from being detected. Additional data in transmission at different wavelengths and/or higher resolution will be required to gain information about these other molecules.

ACKNOWLEDGMENTS

REFERENCES

Agol E., Cowan N. B., Bushong J., Knutson H., Charbonneau D., Deming D., Steffen J. H., 2008, in Pont F., Sasselov D., Holman M., eds, Proc. IAU Symp. 253, Transiting Planets. Cambridge Univ. Press, Cambridge, p. 209
Alard C., 2000, A&AS, 144, 363
Barber R. J., Tennyson J., Harris G. J., Tolchenov R. N., 2006, MNRAS, 368, 1087
Barman T., 2007, ApJ, 661, L191
Batista V. et al., A&A, preprint (arXiv:0907.3471)
Beaulieu J. P., Carey S., Ribas I., Tinetti G., 2008, ApJ, 677, 1343
Bertin E., Arnouts S., 1996, A&AS, 117, 393
Borysow A., Jorgensen U. G., Fu Y., 2001, J. Quant. Spectrosc. Radiative Transfer, 68, 235
Brown T., 2001, ApJ, 553, 1006
Burrows A., Hubeny I., Budaj J., Knutson H. A., Charbonneau D., 2007, ApJ, 668, L171
Carter J. A., Yee J. C., Eastman J., Gaudi B. S., Winn J. N., 2008, ApJ, 689, 499
Charbonneau D., Brown T., Latham D., Mayor M., 2000, ApJ, 529, L45
Charbonneau D., Brown T. M., Noyes R. W., Gilliland R. L., 2002, ApJ, 568, 377
Charbonneau D. et al., 2005, ApJ, 626, 523
Charbonneau D. et al., 2008, ApJ, 686, 1341
Claret A., 2000, A&A, 363, 1081
Cody A. M., Sasselov D. D., 2002, ApJ, 569, 451
Deming D., Seager S., Richardson L. J., Harrington J., 2005, Nat, 434, 740
Désert J. M., Lecavelier des Etangs A., Hébrard G., Sing D. K., Ehrenreich D., Ferlet R., Vidal-Madjar A., 2009, ApJ, 699, 478
Díaz-Cordovés J., Claret A., Giménez A., 1995, A&AS, 110, 329
Dong S. et al., 2009, ApJ, 698, 1826
Doran M., Muller C. M., 2004, J. Cosmol. Astropart. Phys., 9, 3
Ehrenreich D., Hébrard G., Lecavelier des Etangs A., Sing D. K., Désert J. M., Bouchy F., Ferlet R., Vidal-Madjar A., 2007, ApJ, 668, L179
Fazio G. G. et al., 2004, ApJS, 154, 10
Fossey S. J., Waldmann I. P., Kipping D. M., 2009, MNRAS, 396, L16
Fröhlich C., Lean J., 2004, AARv, 12, 273
Gillon M. et al., 2007, A&A, 471, L51
Griffith C. A., Yelle R. V., Marley M. S., 1998, Sci, 282, 2063
Kipping D. M., 2008, MNRAS, 389, 1383
Knutson H. et al., 2007, Nat, 447, 183
Knutson H. et al., 2008, ApJ, 673, 526
Kurucz R., 2006, Stellar Model and Associated Spectra (http://kurucz.harvard.edu/grids.html)
Liang M. C., Parkinson C. D., Lee A. Y. T., Yung Y., Seager S., 2003, ApJ, 596, L247
Liang M. C., Seager S., Parkinson C. D., Lee A. Y. T., Yung Y., 2004, ApJ, 605, L61
Madhusudhan N., Seager S., 2009, ApJ, 707, 24
Mandel K., Algol E., 2002, ApJ, 580, L171
Mayor M., Queloz D., 1995, Nat, 378, 355
Mazeh T. et al., 2000, ApJ, 532, L55
Metcalfe T. S. Charbonneau P., 2003, J. Comput. Phys., 185, 176
Morales-Calderón M. et al., 2006, ApJ, 653, 1454
Nassar R., Bernath P., J. Quant. Spectrosc. Radiative Transfer, 82, 279
Press W. H., Teukolsky S. A., Vetterling W. T., Flannery B. P., 1992, Numerical Recipes in Fortran. The Art of Scientific Computing. Cambridge Univ. Press, Cambridge
Richardson L. J., Deming D., Horning K., Seager S., Harrington J., 2006, Nat, 445, 892
Rothman L. S. et al., 1995, in Proc. Soc. Photo Optical Instrumentation Engineers, Vol. 2471, p. 105
Rothman L. S. et al., 2005, J. Quant. Spectrosc. Radiative Transfer, 96, 139
Schneider J., 2009, The Extrasolar Planets Encyclopaedia, http://exoplanet.eu/index.php
Seager S., Mallen-Ornelas G., 2003, ApJ, 585, 1083
Seager S., Sasselov D. D., 2000, ApJ, 537, 916
Swain M. R., Vasisht G., Tinetti G., 2008, Nat, 452, 329
Swain M. R. et al., 2009a, ApJ, 690, L114
Swain M. R. et al., 2009b, ApJ, 704, 1616
Tashkun S. A., Perevalov V. I., Teffo J.-L., Bykov A. D., Lavrentieva N. N., 2003, J. Quant. Spectrosc. Radiative Transfer, 82, 165
Tinetti G., Beaulieu J. P., 2008, in Pont F., Sasselov D., Holman M., eds, Proc. IAU Symp. 253, Transiting Planets. Cambridge Univ. Press, Cambridge, p. 232
Tinetti G. et al., 2007a, ApJ, 654, L99
Tinetti G. et al., 2007b, Nat, 448, 169
Torres G., Winn J. N., Holman M. J., 2008, ApJ, 677, 1324
Winn J. N. et al., 2005, ApJ, 631, 1215

This paper has been typeset from a T$_E$X/L^{A}T$_E$X file prepared by the author.